Structure of QC_2D ground state fields at nonzero matter densities

Ragib F. Hasan,[1] Matthew Cummins,[1] Waseem Kamleh,[1] Dale Lawlor,[2] Derek B. Leinweber,[1] Ian van Schalkwyk,[1] and Jon-Ivar Skullerud[2]

[1]*Centre for the Subatomic Structure of Matter (CSSM), Department of Physics, Adelaide University, SA, 5005, Australia*

[2]*Department of Physics, Maynooth University–National University of Ireland Maynooth, County Kildare, Ireland*

(Received 30 March 2026; accepted 9 October 2026; published 5 November 2026)

A quantitative investigation into the modification of ground-state field structures in two-color QCD (QC_2D) is presented at finite chemical potential. Using lattice simulations with Wilson gauge and fermion actions, we explore the chromo-electromagnetic field strengths under varying matter densities. To ensure accurate measurements, we develop and calibrate two highly improved topological charge operators and evaluate four gradient flow actions. Our results reveal a finite-volume crossover in the regime of the anticipated phase boundary at $\mu = m_\pi/2$, with both chromoelectric and chromomagnetic field strengths suppressed before recovering and exceeding vacuum values at higher chemical potentials. We find the difference between the squared chromoelectric and chromomagnetic field strengths, $E^2 - B^2$, to increase in magnitude monotonically with increasing chemical potential. At $a\mu = 0.7$, we find an 11% suppression of E^2, a relatively small effect. A systematic analysis using sigmoid fits of lattice simulations in the crossover regime is performed to confirm the critical chemical potential obtained from the field structure is in agreement with the phase boundary at $m_\pi/2$. These findings provide new insight into non-Abelian ground-state vacuum field structures and offer a foundation for future studies in real QCD.

DOI: 10.1103/31cw-ym32

I. INTRODUCTION

The phase structure of strongly interacting matter at high densities, beyond the nuclear saturation density and at low temperatures, remains one of the major unresolved issues in fundamental physics, despite extensive research efforts spanning several decades. Gaining precise insight into this region could help answer key questions about the structure and behavior of compact stars, including whether deconfined quark matter might be present within them.

Progress has been limited because conventional weak-coupling techniques are only applicable at asymptotically high densities, and the various theoretical models used so far lack constraints from experimental data or first-principles calculations. As a result, although numerous models offer insights into potential phases and their characteristics, no undisputed quantitative conclusions have been reached. Lattice QCD simulations could potentially resolve many key questions, but progress is limited by the well-known sign problem [1]. Although progress is being made for QCD itself (for a recent review see Ref. [2]), simulations of QCD-like theories that avoid this issue can offer valuable, non-perturbative insights [3]. The primary objective of this study is to use such simulations to help constrain and inform theoretical models.

Among the various QCD-like theories [4], two-color QCD (QC_2D), which uses the SU(2) gauge group, is particularly noteworthy [3,5–7]. It retains many key features of QCD, such as: confinement, dynamical chiral symmetry breaking, and long-range interactions—while differing in that its baryons are bosons. Notably, the lightest baryon in QC_2D is a pseudo-Goldstone boson, degenerate with the pion. Hence, instead of a conventional nuclear matter phase, this theory exhibits a superfluid state, marked by the condensation of baryons, which become true Goldstone bosons at this point.

The phase structure of QC_2D has been the subject of numerous investigations (see the recent reviews [3,7] for more details), with a clear picture emerging.

At low temperature T and quark chemical potential μ, we find a hadronic phase, characterized by dynamical chiral symmetry breaking and a vanishing Polyakov loop (indicating confinement of static color charges). At high T and small μ, there is a transition to a quark-gluon plasma characterized by chiral symmetry restoration and a non-vanishing Polyakov loop. At finite, nonzero quark mass,

Published by the American Physical Society under the terms of the Creative Commons Attribution 4.0 International license. Further distribution of this work must maintain attribution to the author(s) and the published article's title, journal citation, and DOI. Funded by SCOAP³.

both these transitions are smooth crossovers, and it is not yet determined whether their respective pseudocritical temperatures T_χ and T_d coincide at $\mu = 0$. At low T, as the chemical potential increases, there is a transition to a baryon superfluid state at $\mu = m_\pi/2$, characterized by a nonvanishing diquark condensate $\langle qq \rangle$. The superfluid transition temperature T_Δ is found to be below T_χ and T_d, and almost independent of μ [8,9].

For μ not much above $m_\pi/2$, the superfluid phase is characterized by a Bose-Einstein condensate of tightly bound diquarks, described by chiral perturbation theory [10,11]. As μ increases, there is a crossover to a Bardeen-Cooper-Schrieffer (BCS) regime which may be described by a Fermi sphere of weakly interacting quarks disrupted by a diquark condensate scaling as the area of the Fermi surface, $\langle qq \rangle \sim \mu^2$. Whether or not there is a deconfinement transition at large μ and $T = 0$ remains undecided; the crossover temperature T_d is found to decrease with increasing μ [9,12], but early indications of deconfinement at large μ [13] were later found to be lattice artifacts [9].

A notable feature of the thermodynamics of QC_2D at low T is that the speed of sound c_s exhibits a peak in the superfluid region where it exceeds its high-density (conformal) limit, $c_s^2 = 1/3$ [14]. This feature is also found in isospin-QCD [15], and is inferred from neutron star observations to also be present in real QCD [16,17] (see also [18] for a discussion of the relation between these theories).

Of particular interest is the gluodynamics and ground-state field structures of QC_2D, which may provide direct lessons for real QCD. Like QCD, QC_2D is a non-Abelian gauge field theory enabling gluons to self-interact. This makes the empty vacuum unstable to the formation of quark and gluon condensates which permeate spacetime. These ground-state fields form the foundation of matter and give rise to quark confinement and dynamical chiral symmetry breaking [19].

Although transitioning from QCD to QC_2D fundamentally changes the structure of hadrons, where baryons in QC_2D consist of two valence quarks, the gluonic sector is at most indirectly affected. Studies quantitatively comparing gluon and ghost propagators in SU(2) and SU(3) gauge theory report quantitative agreement between the propagators over a wide range of momenta [20,21], confirming an anticipated infrared independence from the gauge group [22]. This stability allows researchers to explore gluonic observables such as the gluon propagator and string tension [8,12,13,23] within QC_2D, potentially offering valuable insights into their behavior in real QCD. Consequently, studying quantities like the energy density, topological charge density, and the chromoelectric and chromomagnetic field strength densities in QC_2D are of interest.

Topological charge and susceptibility has previously been studied in dense QC_2D by several groups [10,24–27] (see Ref. [28] for an overview of topological aspects of dense matter). For $N_f = 2$ at low temperature, simulations with Wilson fermions find no evidence that the topological susceptibility changes with chemical potential [25,27], while simulations with staggered fermions at somewhat higher temperature find a clear drop for $\mu \gtrsim m_\pi/2$ [10]. A study of the chromoelectric flux tube [29] found that the flux tube persists in the superfluid phase.

This paper complements and extends these studies by exploring how the Euclidean action density, the topological charge density, and the squared chromoelectric and -magnetic field strengths $\langle E^2 \rangle$ and $\langle B^2 \rangle$, respectively, change under the influence of a nonzero matter density. We will focus in particular on $\langle E^2 \rangle$ and $\langle B^2 \rangle$ (which were also studied in Ref. [10]) since we find that these quantities are sensitive to the onset transition at low T.

As these gluonic measures are calculated directly from the vacuum gauge fields, one needs to smooth the gauge fields to suppress otherwise large and uncontrolled renormalizations. Gradient flow is now the accepted standard for gauge field smoothing and this is used herein. However, a number of different implementations have been proposed, drawing on a variety of improvement schemes corresponding to different actions. Four of the most popular schemes are carefully explored herein. The techniques used to select an optimal smoothing are reviewed before presenting our best understanding of how the finite matter density induces changes in the QC_2D ground-state field configurations.

The outline of this paper is as follows. Section II briefly reviews and summarizes the lattice techniques used to implement a finite matter density in QC_2D. We then proceed with a qualitative look at the vacuum field structure and the manner in which a finite matter density changes that structure in Sec. III. Moving toward a quantitative examination, Sec. IV examines the features of various lattice-action improvement schemes, determining a stable action that preserves nonperturbative field structure and quantifying the minimal gradient flow required to extract quantitative results from the gauge-field configurations. Our survey of the impact of a finite matter density on the ground-state field structure of QC_2D are presented in Sec. V. Here we examine the critical chemical potential of the finite-density transition through an inflection-point analysis drawing on additional simulations near the finite-volume crossover. We find the critical chemical potential obtained from changes in the ground-state field structure to coincide with the phase boundary at $m_\pi/2$. A summary of our best understanding of the impact of finite density on the ground-state fields is presented in the conclusions of Sec. VI.

II. FINITE DENSITY IN QC_2D

This study employs the conventional Wilson plaquette gauge action alongside two flavors of Wilson fermions to investigate QC_2D. The fermion sector includes a

gauge- and isospin-singlet diquark source term, j, which serves to lift the low-lying eigenvalues of the Dirac operator. This modification enables a controlled exploration of diquark condensation phenomena [30]. The corresponding quark action is

$$S_Q + S_J = \sum_{i=1,2} \bar{\psi}_i M \psi_i + \kappa j [\psi_2^{\mathrm{tr}} (C\gamma_5)\tau_2 \psi_1 - \mathrm{H.c.}], \quad (1)$$

where tr denotes the transpose, $\kappa = 1/(2m_q + 8r)$ is the hopping parameter for quark mass m_q and Wilson parameter $r = 1$. The matrix C is the charge conjugation matrix, τ_2 is the second Pauli matrix acting in color space, and the fermion matrix M is

$$M_{xy} = \delta_{xy} - \kappa \sum_{\nu} [(1-\gamma_\nu) e^{\mu \delta_{\nu 0}} U_\nu(x) \delta_{y,x+\hat{\nu}} + (1+\gamma_\nu) e^{-\mu \delta_{\nu 0}} U_\nu^\dagger(y) \delta_{y,x-\hat{\nu}}], \quad (2)$$

where γ_ν are the Hermitian gamma matrices. We note here the special role the time component plays in implementing the chemical potential.

To understand the origin of this fermion action, we recall the continuum formulation for noninteracting fermions at temperature T

$$S = \int_0^{1/T} d\tau \int d^3x \bar{\psi}(\gamma_\nu \partial_\nu + m)\psi. \quad (3)$$

To obtain the grand canonical partition function, we add the chemical potential term with number operator N as

$$\frac{\mu N}{T} = \int_0^{1/T} d\tau \int d^3x \mu \bar{\psi} \gamma_4 \psi. \quad (4)$$

Incorporating a gauge field A_ν, the action becomes

$$S = \int_0^{1/T} d\tau \int d^3x \bar{\psi}[\gamma_\nu(\partial_\nu + iA_\nu) + \mu\gamma_4 + m]\psi. \quad (5)$$

Reference [1] highlights several key features of this expression. Notably, μ enters similarly to iA_4, the imaginary-time component of a four-vector field. This suggests that finite-density effects may manifest in the temporal direction, potentially revealing differences between chromoelectric and chromomagnetic fields.

Additionally, at $\mu = 0$, the Dirac operator satisfies γ_5-Hermiticity

$$(\gamma_5 M)^\dagger = \gamma_5 M \;\Rightarrow\; M^\dagger = \gamma_5 M \gamma_5, \quad (6)$$

which implies

$$\det(M^\dagger) = \det(\gamma_5 M \gamma_5) = \det M = (\det M)^* \quad (7)$$

and hence the determinant is real. However, for $\mu \neq 0$,

$$M^\dagger(\mu) = \gamma_5 M(-\mu^*)\gamma_5, \quad (8)$$

and

$$(\det M(\mu))^* = \det M(-\mu^*) \in \mathbb{C}. \quad (9)$$

In general, this can lead to a complex probability weight known as the sign problem, obstructing importance sampling.

In two-color QC$_2$D [31], the absence of the sign problem comes from the special property that the fundamental representation of SU(2) is pseudoreal [4,32]. This means that quarks and antiquarks are related in a way that ensures the Dirac operator, even with a finite chemical potential, is always mapped to its complex conjugate by a similarity transformation. As a result, the eigenvalues of the Dirac operator occur in complex-conjugate pairs, which ensures the fermion determinant remains real. For an even number of quark flavors, the determinant is also non-negative, so the path integral measure can still be interpreted probabilistically.

A naïve attempt to add $\mu\bar{\psi}\gamma_4\psi$ directly to the lattice action results in ultraviolet divergences. Instead, inspired by the continuum analogy, one treats μ as the imaginary component of an Abelian vector field in the temporal direction. This leads to the introduction of the chemical potential in the temporal hopping terms [1,33,34] of Eq. (2), ensuring that forward-moving quarks in time are favored, while backward-moving ones are suppressed, creating an asymmetry in temporal propagation.

The chemical potential represents the free energy required to introduce a particle into the system. Consequently, in QC$_2$D, observable changes are expected when μ reaches half of the diquark baryon mass, m_b. As μ is associated with a single quark and baryons have two quarks (in QC$_2$D), $\mu_C = m_b/2 = m_\pi/2$ as $m_b = m_\pi$ in QC$_2$D. Due to this degeneracy with the pion mass, $m_\pi/2$ marks the onset of particle creation from the vacuum and potential structural changes in the ground-state vacuum fields.

In this work we will be using the "Coarse" ($\beta = 1.9$, $\kappa = 0.1680$) and "Fine" ($\beta = 2.1$, $\kappa = 0.1577$) lattice ensembles described in Ref. [9]. We use the lowest-temperature lattices for each ensemble, with lattice volumes of $16^3 \times 24$ and $16^3 \times 32$, respectively, both corresponding to temperatures $T \approx 40$ MeV. The lattice spacings, set by the string tension of $\sqrt{\sigma} = 440$ MeV, are $a = 0.178(6)$ fm and $a = 0.130(1)$ fm [35], respectively, with pion masses $am_\pi = 0.645(8)$ and $am_\pi = 0.446(3)$, respectively, both corresponding to a pion mass $m_\pi \approx 700$ MeV.

III. FIRST LOOK AT FINITE DENSITY FIELD MODIFICATION

We begin by visualizing the action density, topological charge density and distributions of the squared chromo-electric and -magnetic fields strengths, $E^2(x)$ and $B^2(x)$, respectively, on representative gauge field configurations. The five-loop $\mathcal{O}(a^4)$-improved lattice field-strength tensor [36] is used to determine these from the lattice gauge fields.

We consider the vacuum field structure on the $\beta = 1.9$, $\kappa = 0.1680$ lattices at $a\mu = 0$ and contrast this with a representative $a\mu = 0.4$ configuration above the phase boundary at $am_\pi/2 = 0.323(4)$. This is then compared with a representative $a\mu = 0.7$ configuration, where lattice artifacts associated with large $a\mu$ are expected to be benign. We seek to observe qualitative changes in the vacuum field structure.

To suppress short distance fluctuations in exposing the longer distance nonperturbative structures in the gauge fields, we implement a standard gradient flow and illustrate the field structures at a moderate gradient flow time of $t_g = 2.4$. To see into the 3D volume, a threshold is set such that field values below the threshold are not rendered. In all cases of comparison, the threshold is held fixed.

As the Euclidean time dimension is unique at finite density, it is important to include this dimension in the visualizations. Accordingly, we slice the four-dimensional volume at constant values of the x coordinate to render a 3D perspective. Thus the visualizations illustrate the y, z and t variation of the field structure. The time direction is easily identified as the elongated axis with 24 units with respect to the other axes of length 16. While many configurations and many different x coordinates were examined, the visualizations presented here are selected as good representatives of our general observations.

The left column of Fig. 1 shows the action densities of three configurations at the aforementioned three chemical potentials. The corresponding topological charge densities are illustrated in the right column. Despite very large differences in the chemical potentials considered in generating these configurations, the renderings are qualitatively similar, confirming early expectations that the vacuum structure modification is subtle [23,25]. In a blind test, it would be very difficult to tell these configurations apart. Studies of the topological susceptibility also indicate an insensitivity to the chemical potential [11,27].

Figure 2 illustrates the squared field strengths, $E^2(x)$ and $B^2(x)$, for the same three configuration slices. It is difficult by direct comparison to tell these fields apart with both maintaining approximately the same shape of objects. To more clearly see the difference in $E^2(x)$ and $B^2(x)$, we visualize $E^2(x) - B^2(x)$ in the right-most column of Fig. 2. Here we finally observe a qualitative impact of the chemical potential on the ground-state field structure. The large chemical potential configurations show an abundance of violet/blue revealing a qualitative-level impact of the chemical potential on the balance of $E^2(x)$ and $B^2(x)$.

Thus, the nonzero chemical potential has indeed impacted the vacuum balance of chromo-electromagnetic field strengths. This signature demands a quantitative analysis to learn the nature of the dynamics. In proceeding to do this, we will examine the utility of several improved gauge actions under consideration for the gradient flow. We will also construct alternative improved operators for the topological charge density and use this as a measure of systematic errors in the determinations of the chromo-electromagnetic field strengths. With these improvements in hand we will determine the minimal gradient flow required to determine the fields and discover the impact of the chemical potential on the ground-state fields.

IV. LATTICE-ACTION IMPROVEMENT IN THE GRADIENT FLOW

A. Highly improved operators for measuring ground-state field strengths

On the original Monte Carlo generated configurations, the lattice field strength tensor operators encounter renormalization factors far from unity. The application of gradient flow significantly suppresses the ultraviolet fluctuations and brings the renormalization factors toward 1. This process rapidly alters the lattice field strengths within just a few updates. As a result, determining the optimal flow time for analyzing the field strengths becomes a nuanced challenge.

The results of the previous Section place our focus on the squared chromo-electromagnetic field strengths, $E^2(x)$ and $B^2(x)$, and their differences. To determine the gauge field smoothness required to accurately determine these field strengths, we focus on the topological charge density, $q(x)$. As $E^2(x)$, $B^2(x)$ and $q(x) \propto \vec{E}(x) \cdot \vec{B}(x)$ are all constructed from the same flowed lattice field strength tensor, the topological charge density provides a single operator that is sensitive to both the chromoelectric and -magnetic field flows.

To determine the flow time where discretization artifacts in the flowed field strength tensor are sufficiently small, we follow the ideas introduced in Ref. [37] and consider two highly-improved measures of the topological charge density. One approach improves the lattice field strength tensor first [36] and then derives the topological charge density from this refined operator; we call this estimate the "Improved $F_{\mu\nu}$" density, $q_F(x)$. The alternative method directly improves the topological charge density itself [38], referred to as the "Direct" density, $q_D(x)$. Although both techniques yield $\mathcal{O}(a^4)$-improved estimates of the topological charge density, they differ significantly in their $\mathcal{O}(a^6)$ error structures. Our objective is to identify the regime where these discrepancies become negligible, enabling controlled measurements of the chromoelectric and chromomagnetic field strengths.

Here we briefly summarize the construction of these two distinct $\mathcal{O}(a^4)$-improved topological charge operators,

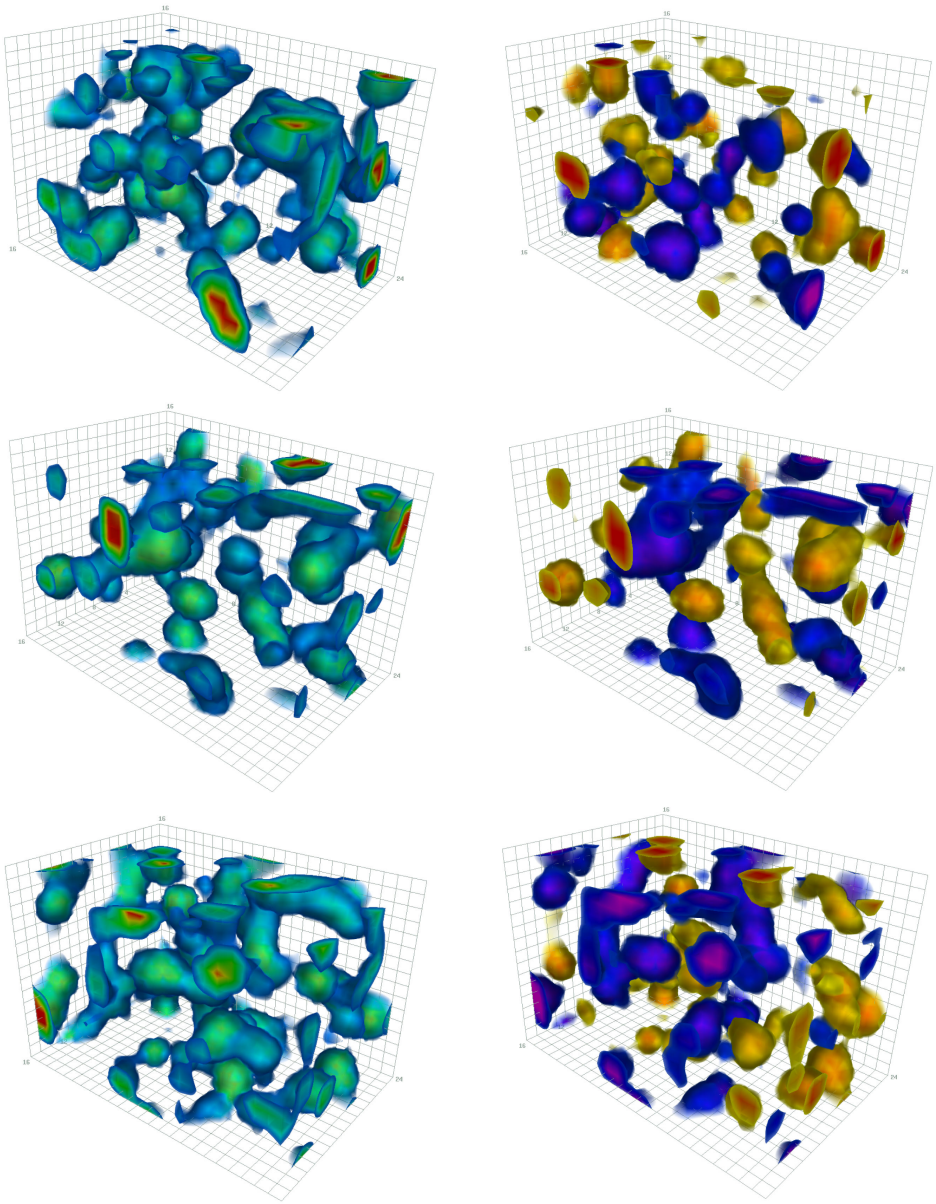
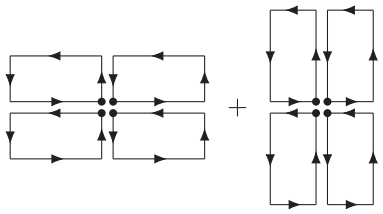


FIG. 1. Comparison of the action density (left column) and topological charge density (right column) illustrated for chemical potentials of $a\mu = 0$ (top), $a\mu = 0.4$ (middle) and $a\mu = 0.7$ (bottom). For the action density in the left column, red/yellow/green/blue shading indicates high to low local action density. Similarly, for the topological charge density in the right column, violet/blue indicates negative topological charge density and red/yellow indicates positive topological charge density, with violet and red illustrating the largest magnitudes. The lowest action and topological-charge density regions below their respective thresholds are not rendered as described in the text.

using the conventions presented in Ref. [37]. The first operator, termed the "Improved $F_{\mu\nu}$" scheme [$q_F(x)$], is constructed by inserting an $\mathcal{O}(a^4)$-improved field strength tensor into the topological charge definition

$$q(x) = \frac{g^2}{32\pi^2}\epsilon_{\mu\nu\rho\sigma}\mathrm{Tr}(F_{\mu\nu}(x)F_{\rho\sigma}(x)). \tag{10}$$

The $m \times n$ clover term $\mathcal{C}_{\mu\nu}^{(m\times n)}(x)$ is defined as the sum of $m \times n$ and $n \times m$ Wilson loops in the μ-ν plane at the point x

$\mathcal{C}_{\mu\nu}^{(m\times n)} =$  . (11)

Each clover term estimates the field strength tensor as

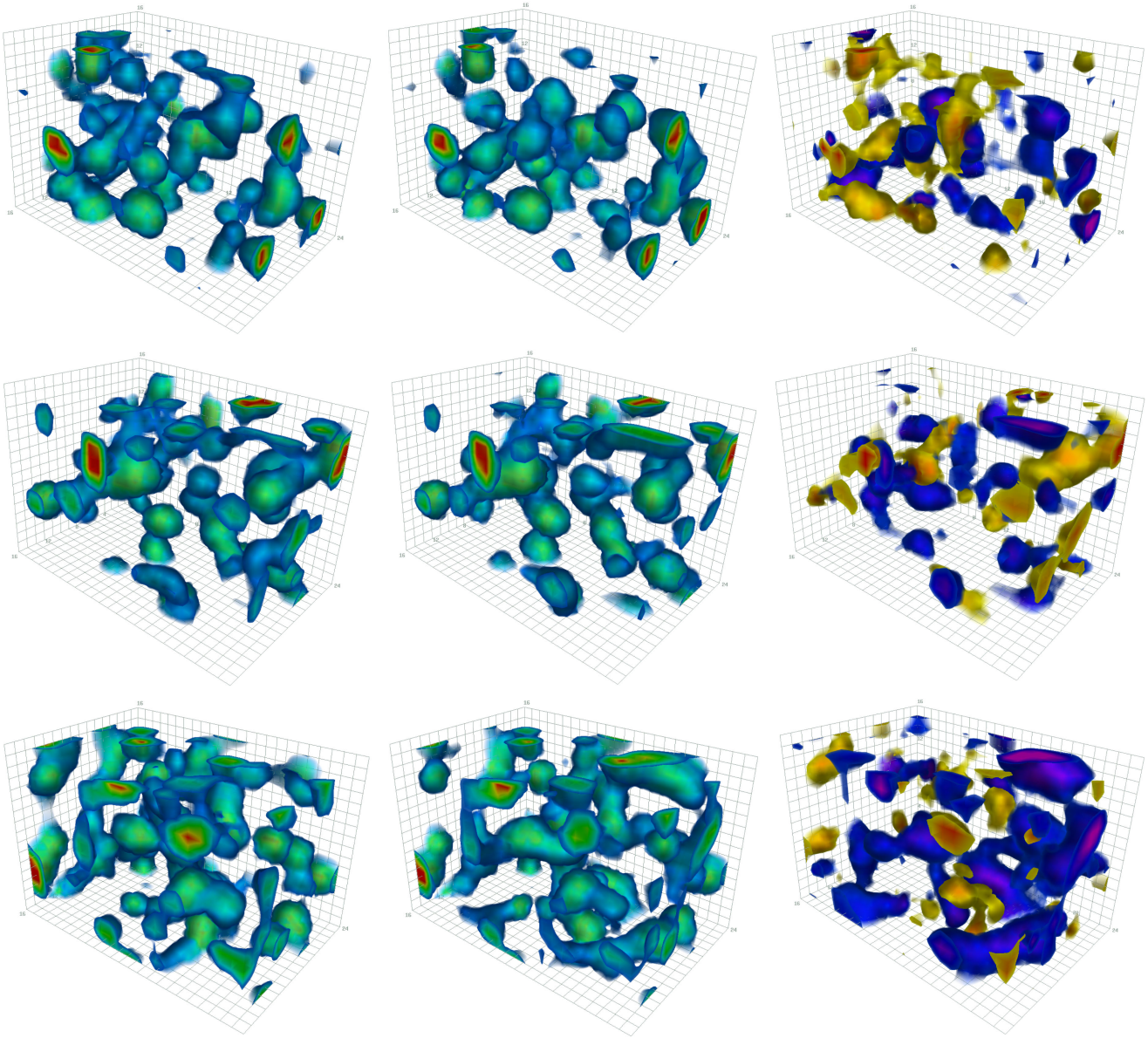


FIG. 2. Comparison of squared chromoelectric field, $E^2(x)$ (left column), the squared chromomagnetic field, $B^2(x)$ (middle column), and the difference, $E^2(x) - B^2(x)$ (right column) for chemical potentials of $a\mu = 0$ (top row), $a\mu = 0.4$ (middle row) and $a\mu = 0.7$ (bottom row). Color shadings for the positive squared field strengths, $E^2(x)$ and $B^2(x)$, are as for the action density of Fig. 1. The difference $E^2(x) - B^2(x)$ has both positive and negative values and is rendered in the same manner used for the topological charge in Fig. 1. Thus, violet/blue indicates a negative value [i.e., $B^2(x) > E^2(x)$] and red/yellow indicates a positive value [i.e., $E^2(x) > B^2(x)$]. An abundance of violet/blue in the bottom right plots reveals an impact of the chemical potential on the balance of $E^2(x)$ and $B^2(x)$.

$$F_{\mu\nu}^{(m\times n)}(x) = \frac{1}{8}\mathrm{Im}(C_{\mu\nu}^{(m\times n)}(x)). \tag{12}$$

The improved operator is then formed by a linear combination

$$ga^2 F_{\mu\nu}(x) = \sum_{m,n} k^{(m\times n)} F_{\mu\nu}^{(m\times n)}(x). \tag{13}$$

To cancel $\mathcal{O}(a^2)$ and $\mathcal{O}(a^4)$ errors, $(m,n) = (1,1)$, (2,2), (1,2), (1,3), and (3,3) are considered with coefficients

$$\begin{aligned} k^{(1\times 1)} &= \frac{19}{9} - 55\,k^{(3\times 3)}, \\ k^{(2\times 2)} &= \frac{1}{36} - 16\,k^{(3\times 3)}, \\ k^{(1\times 2)} &= -\frac{32}{45} + 64\,k^{(3\times 3)}, \\ k^{(1\times 3)} &= \frac{1}{15} - 6\,k^{(3\times 3)}, \end{aligned} \tag{14}$$

with $k^{(3\times 3)}$ as a free parameter [36].

Alternatively, one can define a set of discretized topological charge operators $q^{(m\times n)}(x)$ for each clover term [38]

$$q^{(m\times n)} = \frac{1}{32\pi^2}\frac{1}{m^2n^2}\varepsilon_{\mu\nu\rho\sigma}\mathrm{Tr}(F^{(m\times n)}_{\mu\nu}F^{(m\times n)}_{\rho\sigma}). \quad (15)$$

Here, $F^{(m\times n)}_{\mu\nu}(x)$ is as before. These can be combined into another improved operator

$$q_D(x) = \sum_{m,n} c^{(m\times n)} q^{(m\times n)}(x). \quad (16)$$

This is the "Direct" improvement scheme ($q_D(x)$). Since $q(x)$ is nonlinear in $F_{\mu\nu}$, the two schemes will have different $\mathcal{O}(a^6)$ errors. Using the same five clover terms, the coefficients which cancel $\mathcal{O}(a^2)$ and $\mathcal{O}(a^4)$ errors are

$$\begin{aligned} c^{(1\times1)} &= \frac{1}{9}(19 - 55\,c^{(3\times3)}),\\ c^{(2\times2)} &= \frac{1}{9}(1 - 64\,c^{(3\times3)}),\\ c^{(1\times2)} &= \frac{1}{45}(-64 + 640\,c^{(3\times3)}),\\ c^{(1\times3)} &= \frac{1}{5} - 2\,c^{(3\times3)}. \end{aligned} \quad (17)$$

These match the coefficients used in constructing an improved action from the same loops [38,39].

To compare the schemes, we examine three-loop and five-loop versions of both. The three-loop versions use $k^{(3\times3)} = 1/90$ and $c^{(3\times3)} = 1/10$, such that the 1×2 and 1×3 loops do not contribute. The five-loop versions use $k^{(3\times3)} = 1/180$ [36] and $c^{(3\times3)} = 1/20$ [38,39].

We have compared the three-loop and five-loop schemes for both $q_F(x)$ and $q_D(x)$. For each, we compute the total sum of the absolute topological charge density $Q = \sum|q(x)|$ and the relative error

$$R_E = \frac{|Q_F - Q_D|}{\frac{1}{2}(Q_F + Q_D)}. \quad (18)$$

Our calculations show that the five-loop improvement schemes are more consistent than the three-loop schemes. Thus, we utilize the five-loop versions of both $q_F(x)$ and $q_D(x)$ as our benchmark for identifying when optimal smoothing is achieved.

B. Gradient flow

The Yang-Mills gradient flow [40] evolves the gauge field $A_\mu(x)$ into a flowed field $A_\mu(x,t)$ via a diffusion equation in flow time t

$$\frac{d}{dt}A_\mu(x;t) = -\frac{\delta S}{\delta A^a_\mu(x;t)}t^a = D_\nu F_{\nu\mu}(x;t), \quad (19)$$

with

$$A_\mu(x;t) = A^a_\mu(x;t)t^a, \quad \text{and} \quad A_\mu(x;t=0) = A_\mu(x). \quad (20)$$

The t^a are the generators of SU(N) gauge theory, $F_{\mu\nu} = \partial_\mu A_\nu - \partial_\nu A_\mu + [A_\mu, A_\nu]$ is the field strength of the flowed field, and $D_\mu = \partial_\mu + [A_\mu, \cdot]$ is the flow-time covariant derivative, the dot denoting the argument on which D_μ acts.

The smeared gauge field is the solution to this differential equation for $t > 0$. The links evolve in the direction of steepest descent in the action and the action is monotonically decreasing in flow time. The flow is gauge covariant and its diffusive character smooths the gauge field over a physical radius $d = \sqrt{8t}$, exponentially damping momentum modes above the scale $\mu = 1/d$.

On the lattice we work with the dimensionless flow time $t_g \equiv t/a^2$, such that the physical flow time is $t = t_g a^2$ and the physical smoothing radius is $d = \sqrt{8t} = \sqrt{8t_g a^2}$. The flow is implemented with reference to the flowed link variables $U_\mu(x;t)$, and their associated gauge action $S[U]$. Equation (19) takes the form

$$\frac{d}{dt_g}U_\mu(x;t_g) = -ig^2t^a\nabla^a_{x,\mu}S[U]U_\mu(x;t_g), \quad (21)$$

where

$$\nabla^a f(U) = \lim_{\epsilon\to0}\frac{f(\exp(i\epsilon t^a)U) - f(U)}{\epsilon}. \quad (22)$$

The functional derivative is evaluated for a general improved action with the result

$$t^a\nabla^a_{x,\mu}S[U] = -\frac{\beta}{2N}Q_\mu(x), \quad (23)$$

where

$$Q_\mu(x) = \frac{i}{2}\left[(\Omega_\mu(x) - \Omega^\dagger_\mu(x)) - \frac{1}{N}\mathrm{tr}(\Omega_\mu(x) - \Omega^\dagger_\mu(x))\right], \quad (24)$$

is the Hermitian traceless matrix familiar from stout-link smearing [41], built from the link products

$$\Omega_\mu(x) = U_\mu(x)\sum_{\nu\neq\mu}\Sigma_{\mu\nu}(x), \quad (25)$$

with the staples $\Sigma_{\mu\nu}(x)$ associated with the link $U_\mu(x)$, defined by the local action

$$S_{\mathrm{local}}[U_\mu(x)] = -\frac{\beta}{N}\sum_{\nu\neq\mu}\mathrm{Re\,tr}[U_\mu(x)\Sigma_{\mu\nu}(x)], \quad (26)$$

for SU(N) gauge field theory. Thus

$$\frac{d}{dt_g}U_\mu(x;t_g) = iQ_\mu(x;t_g)U_\mu(x;t_g). \tag{27}$$

Gradient flow is a continuous realization of stout-link smearing. Numerical integration of the gradient flow is performed via

$$U_\mu(x;t_g+\rho) = \exp\left(i\rho Q_\mu(x;t_g)\right)U_\mu(x;t_g). \tag{28}$$

The finite transformation generated by gradient flow after flow time $t_g = n_s\rho$ is equivalent to stout-smeared links after n_s sweeps for sufficiently small increments ρ.

Our implementation of the gradient flow uses the standard four-dimensional stout-link smearing algorithm of Ref. [41], annealed to effectively update one link at a time, i.e., sequential single-link updates within each sweep, as opposed to a simultaneous update of all links. Our parallel algorithm implements this with link updates uniformly spread throughout the lattice volume [42]. Throughout this quantitative analysis, we use a small isotropic smearing parameter of $\rho = 0.005$. The gradient flow time is $t_g = n_s\rho$, where n_s denotes the number of sweeps of stout-link smearing over the lattice. In conveying the extent of smearing in the following, we refer to the number of sweeps, n_s, or the associated gradient flow time, t_g, interchangeably.

C. Gradient flow actions

Here we present how the optimal improved gradient-flow action and its associated optimal flow time is determined. Historically the simple plaquette gauge-field action was used to define the gradient flow. However, more recently improved gauge-field actions are being considered [43]. These include the $\mathcal{O}(a^2)$-improved Symanzik gauge action [44], the well known Iwasaki action [45] and the doubly blocked from Wilson action in two-coupling space (DBW2) action [46].

In addition to these we will consider an overimproved [47] action which we will refer to as the Moran [48] action. This particular action was designed to stabilize instantons under smoothing. Whereas the Symanzik improved action will shrink instantons under smoothing, the Iwasaki and DBW2 actions will grow instantons under smoothing. For the DBW2 action, we anticipate rapid growth in the size of topological objects within the gauge fields. While we anticipate the Moran action may prove to be optimal for the gradient flow, we also introduce an intermediate gauge field action that bridges the gap between the Moran and Iwasaki actions.

All of these gauge field actions may be succinctly described in a single equation. Here we closely follow the notation of Ref. [48]. They decided to use the traditional combination of plaquettes and rectangles, defined as

$$S(\epsilon) = \beta\sum_x\sum_{\mu>\nu}\left[\frac{5-2\epsilon}{3}(1-P_{\mu\nu}(x)) - \frac{1-\epsilon}{12}\left((1-R_{\mu\nu}(x))+(1-R_{\nu\mu}(x))\right)\right]. \tag{29}$$

Here $P_{\mu\nu}$ is the standard plaquette in the $\mu-\nu$ plane. It includes taking $1/2$ of the real part of the trace of the product of the SU(2) links around the elementary plaquette located at space-time site x. Similarly $R_{\mu\nu}$ refers to link products around 1×2 rectangles. The consideration of both $R_{\mu\nu}$ and $R_{\nu\mu}$ ensures both rectangle orientations are considered.

Note that the ϵ parameter in Eq. (29) has been designed such that $\epsilon = 1$ gives the standard Wilson action, and $\epsilon = 0$ results in the Symanzik $\mathcal{O}(a^2)$-improved action [48]. More generally, the action may be written as

$$S(\epsilon) = \beta\sum_x\sum_{\mu>\nu}\left[C_p(1-P_{\mu\nu}(x)) - C_r\left((1-R_{\mu\nu}(x))+(1-R_{\nu\mu}(x))\right)\right]. \tag{30}$$

For given C_r and C_p coefficients, the ϵ parameter is given by

$$\epsilon = \frac{1-20\frac{C_r}{C_p}}{1-8\frac{C_r}{C_p}}. \tag{31}$$

Table I summarizes the ϵ values associated with the different gradient flow actions under consideration.

Here we emphasize how the Symanzik improved action with $\epsilon = 0$ has an $\mathcal{O}(a^4)$ error that causes instantons to shrink in size under smoothing algorithms. Moran *et al.* [48] introduced the epsilon parameter to over improve the action and change the sign of the error term for instantons. By using a small negative value for ϵ the size of instantons is stabilized under smoothing.

These observations lead to some concern in using the Iwasaki or DBW2 actions within the gradient flow algorithm. Both actions have negative ϵ values, but the magnitude of the values is relatively large. The concern is that large discretization errors in the lattice action will

TABLE I. Plaquette (C_p) and rectangle (C_r) coefficients as defined in Eq. (30) for different gradient flow actions and their corresponding ϵ values.

Gradient flow	C_p	C_r	ϵ
Wilson	1.0000	0.0000	1
Symanzik	1.6667	0.0833	0
Moran	1.8333	0.1042	−0.25
Intermediate	2.3333	0.1667	−1
Iwasaki	3.6480	0.3310	−2.972
DBW2	12.2704	1.4088	−15.9056

enable the gauge field action to be reduced by growing the size of instantons. Thus we are concerned that the Iwasaki and DBW2 actions may not be ideal for preserving the topological structure of the gauge fields. Indeed the renormalization issues that lead to these actions will be removed under gradient flow, making their selection for smoothing poorly motivated.

To fill the gap between the Moran and Iwasaki values for ϵ in Table I, we also include an intermediate action with $\epsilon = -1$.

D. Smoothing criteria

The criterion used in this research to determine the optimal smoothing is the dimensionless quantity defined as

$$\mathcal{F} = t_g^2 \langle |q(x)| \rangle_x. \tag{32}$$

Here t_g is the gradient flow time and $\langle |q(x)| \rangle_x$ is the magnitude of the topological charge density averaged over the lattice sites x. Recalling that the topological charge density has units of GeV^4, and the gradient flow has a physical smoothing distance $d = \sqrt{8t_g}$ [40], this gradient flow measure, $\mathcal{F}$, is dimensionless.

It can be deduced from Eq. (32) that the derivative of $\mathcal{F}$ is linear in t_g when $\langle |q(x)| \rangle_x$ is constant. Reductions in $\langle |q(x)| \rangle_x$ will flatten the curve, so early in the smearing, flattening of the first derivative (i.e., negative values for the second derivative) is a sign that the gradient flow is efficiently removing topological charge density in a local manner. This is the optimal phase where the gauge fields are smoothed with minimal changes in the long-distance field structure. Thus, there is no need to stop smoothing until the first derivative approaches its long term general trend. In the long term general trend, $\langle |q(x)| \rangle_x$ approaches a constant and we enter a phase where opposite-charge topological objects are migrating toward each other and eventually annihilating. The process of annihilation will induce ripples into the dimensionless quantity $\mathcal{F}$ as rapid changes in the topological charge density magnitude take place. In this phase, smoothing is changing the structure of the fields.

We commence our analysis by considering a survey of chemical potential, μ, and source term strengths, j, on the fine ensemble ($\beta = 2.1$, $\kappa = 0.1577$). These lattices are relatively smooth in comparison to the coarse ensemble lattices that will be used later for examining the chemical potential dependence of the ground-state field structure.

In calculating the topological charge density for $\mathcal{F}$, we consider both of the improved measures discussed in Sec. IV A. In the following discussion our attention will be on the topological charge density obtained through the improvement of the lattice field strength tensor. Results from this measure will be compared with the direct improvement of the topological charge density. As we will see, results from the improved lattice field strength tensor will show more structure in the gradient flow, and this is helpful in deriving a stopping criterion for the threshold amount of gradient flow.

Our survey of μ and j values revealed little sensitivity, and the selection of any parameter values may be regarded as representative. Figure 3 shows how the gradient flow measure $\mathcal{F}$ changes for the four gradient flow actions under consideration. In this case we have selected $\mu = 0$. All four plots show a sharp rise in the first derivative of $\mathcal{F}$ at the earliest flow times. Setting the DBW2 action aside, the other three actions then show a flattening of the first derivative. As described earlier, this indicates significant reduction in the topological charge density magnitude. It is here that one aims to continue smoothing as the gradient flow is efficiently removing local fluctuations. However, this flattening is seen to end fairly rapidly. The Moran gradient flow leaves the flattening phase at $t_g \approx 0.6$, the Intermediate gradient flow departs at $t_g \approx 0.5$, and the Iwasaki gradient flow leaves at $t_g \approx 0.4$.

At this point, one enters the long term trend seen over a wide range of gradient flow time. It is here that one becomes concerned that the structure of the gauge fields is being significantly modified through the gradient flow and thus this region is to be avoided. The DBW2 gradient flow never quite flattens out the derivative curve, possibly because the instantons grow very quickly and start annihilating immediately after the flow begins.

There is another important observation to be drawn from Fig. 3. As the magnitude of ϵ increases, the gradient flow criterion, $\mathcal{F}$, becomes increasingly smooth. This is in accord with expectations as emphasized earlier. Large values of ϵ will cause the instantonlike topological objects to grow in size. For large gradient flow time, the objects are likely to become quite large and overlapping. This contrasts the Moran action which is designed to leave the topological structures intact and unaltered under the smoothing algorithm. In this case one can imagine well-defined objects moving across the lattice and occasionally finding neighbors to annihilate with. It is here that large changes in the topological charge density will take place and we will observe ripples in the smoothing criterion, $\mathcal{F}$.

In light of this, it is tempting to discard all actions other than the Moran action. However, the Iwasaki action is well known; it is currently being used within the literature to perform the gradient flow; it does show the fluctuations associated with well-defined objects. Therefore, we feel it will be informative to investigate this gradient flow action further. However, the DBW2 action is not a useful gradient flow action for this research.

Therefore, Moran and Iwasaki are selected to study QC_2D further. The Intermediate gradient flow is dropped since it shows no advantage over the Moran action.

E. Gradient flow effect on coarse lattices

The SU(2) configurations available for the study of the finite-density chemical-potential impact on the

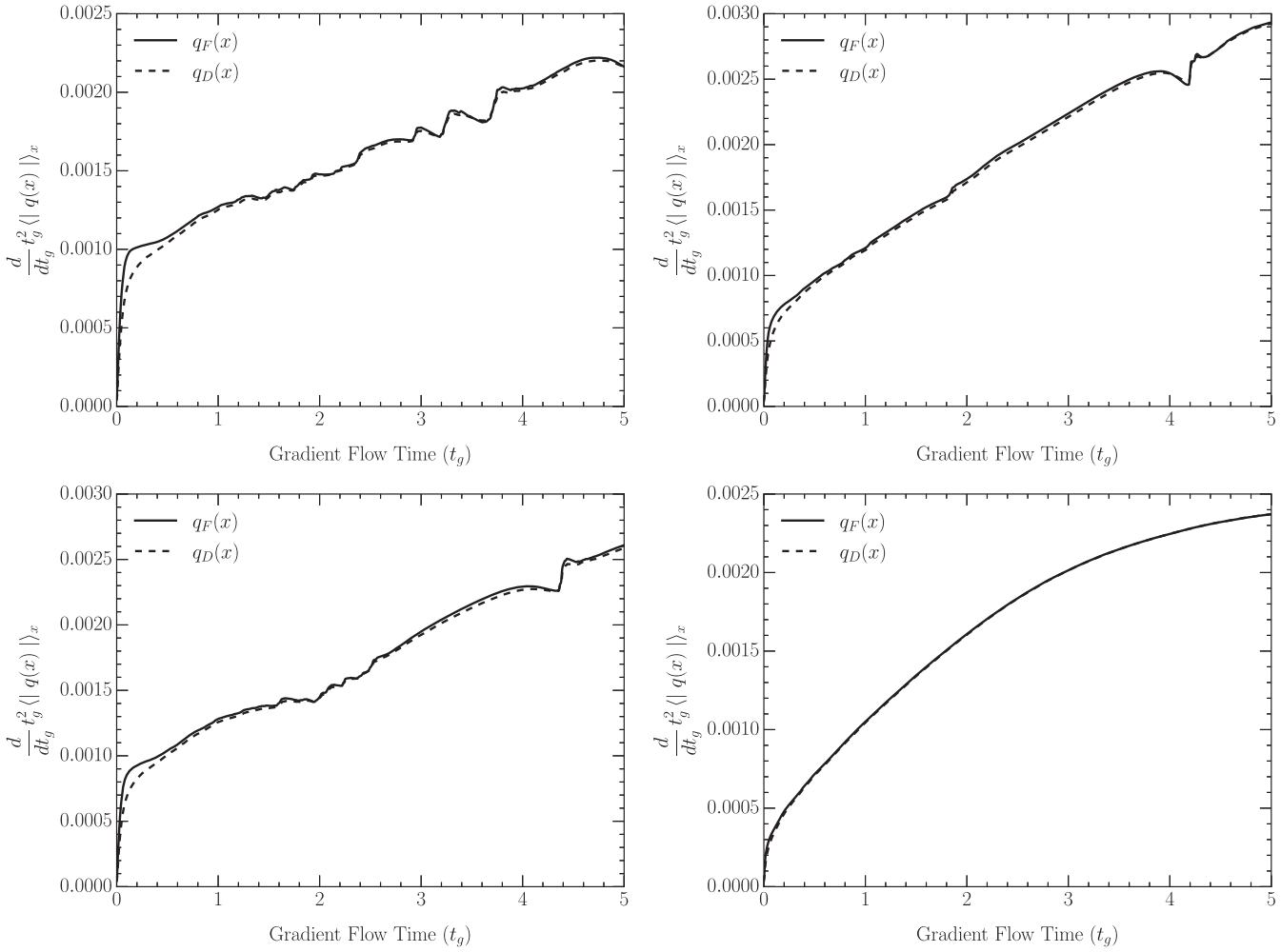


FIG. 3. Representative plots of one configuration with zero chemical potential illustrating the first derivative of $\mathcal{F}$ for the four gradient flow actions: Moran (top left), Intermediate (bottom left), Iwasaki (top right) and DBW2 (bottom right).

ground-state field structure are the coarse ensemble with $\beta = 1.9$ and $\kappa = 0.1680$, providing a lattice spacing of $a = 0.178(6)$ fm [30]. Representative plots for the gradient flow results analogous to Fig. 3 are provided in Fig. 4 for our two preferred gradient-flow actions. The more coarse nature of the lattice spacing presents new

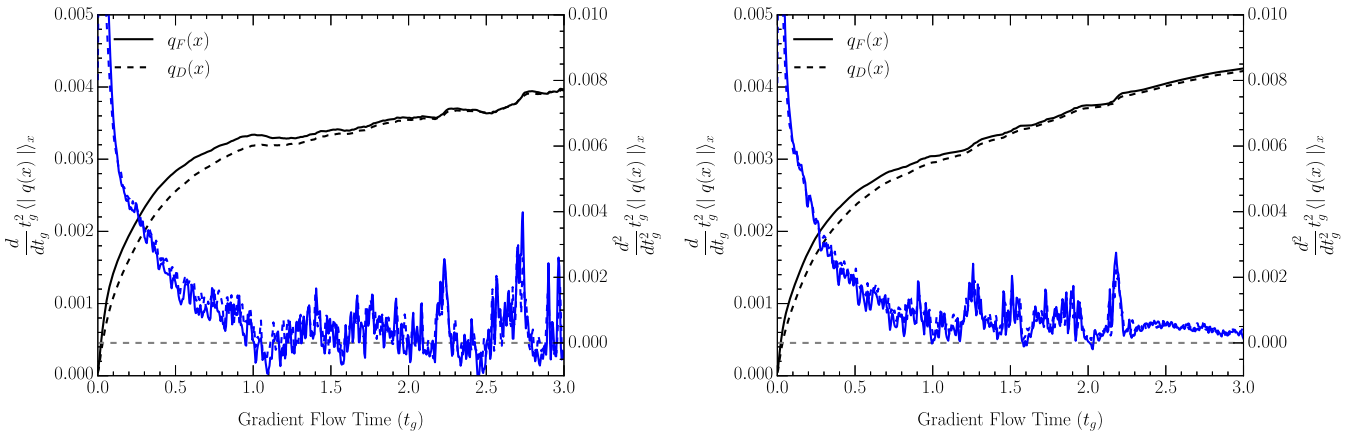


FIG. 4. Representative gradient flows for a coarser $16^3 \times 24$ lattice with $a\mu = 0.25$ and $aj = 0.2$. Both the first derivative (black lines) and second derivative (blue lines) of $\mathcal{F}$ are illustrated for Moran (left) and Iwasaki (right) gradient flows.

challenges in identifying the threshold regime for the gradient flow time. Thus, the second derivative of $\mathcal{F}$ is added in the plots to aid in making a precise determination of the flattening of the first derivative curve on these coarser lattices.

As seen in Fig. 4, the Moran gradient flow enters the long-term trend at $t_g \approx 1.0$ and the Iwasaki gradient flow enters a little earlier at $t_g \approx 0.8$. These flow times correspond to 200 (Moran) and 160 (Iwasaki) sweeps of stout-link smearing with $\rho = 0.005$, respectively.

F. Highly improved topological charge operators

To further examine the nature of the gradient flow, we examine the difference between the two highly improved estimates of the topological charge density presented in Sec. IV A. Recall that one measure first improves the lattice field strength tensor and then constructs the topological density from this improved operator; we refer to this estimate as $q_F(x)$. The other measure directly improves the topological density and is referred to as $q_D(x)$. While both schemes provide an $\mathcal{O}(a^4)$-improved measure of the topological charge density, the $\mathcal{O}(a^6)$ errors are different. Our goal is to understand where these differences are sufficiently small such that we can measure the chromo-electric and chromomagnetic field strengths in an accurate manner.

We introduce a relative error defined by

$$R_E = \frac{\langle |q_F(x)| \rangle_x - \langle |q_D(x)| \rangle_x}{\frac{1}{2}(\langle |q_F(x)| \rangle_x + \langle |q_D(x)| \rangle_x)}, \tag{33}$$

where we once again work with the average magnitudes of topological charge density obtained from the improved lattice field strength tensor operator and the direct topological density operator. Table II tabulates the relative errors between these operators at 120 sweeps of Moran and Iwasaki gradient flows for both the $\beta = 2.1$ and $\beta = 1.9$ ensembles, respectively. It also records the number of sweeps taken for the relative error to drop below 10%. Drawing on this last criterion, in concert with the results of Sec. IV E focusing on the dimensionless flow parameter, $\mathcal{F}$, the optimal sweep numbers for the $\beta = 1.9$ ensemble are determined as 200 (Moran) and 150 (Iwasaki). These sweep numbers correspond to gradient flow times of 1.00 (Moran) and 0.75 (Iwasaki).

We have also considered the Euclidean action remaining for each of these flows using an action constructed from the improved field strength tensor. We find 200 sweeps of Moran gradient flow corresponds to 154 sweeps of the Iwasaki flow, confirming our expectations. Thus, our flow selections are providing a similar field structure.

TABLE II. Performance of the two preferred gradient flow actions on the fine $16^3 \times 32$ lattices with $\beta = 2.1$ and $\kappa = 0.1577$ and the coarse $16^3 \times 24$ lattices with $\beta = 1.9$ and $\kappa = 0.1680$. The gradient flow is quantified by examining the differences between the two $\mathcal{O}(a^4)$-improved topological charge density measures. The relative error defined in Eq. (33) at the 120th sweep (Error_{120}) is indicated in percent, and the number of sweeps required to reduce the error to less than 10% (Sweeps for $< 10\%$) are indicated. The values quoted are the median values observed in a small set of test runs as described in the text, with the uncertainties (in the last digit) given by the deviation of the upper and lower values from the median.

Flow	β	κ	$a\mu$	Err_{120}	Sweeps for $< 10\%$
Moran	2.1	0.1577	0.0	10.5^{+2}_{-3}	127^{+4}_{-4}
			0.4	10.3^{+1}_{-4}	124^{+2}_{-5}
			0.7	10.6^{+3}_{-2}	129^{+4}_{-2}
Iwasaki	2.1	0.1577	0.0	7.4^{+2}_{-3}	85^{+2}_{-3}
			0.4	7.1^{+4}_{-3}	83^{+1}_{-3}
			0.7	7.5^{+2}_{-1}	86^{+3}_{-2}
Moran	1.9	0.1680	0.0	15.0^{+1}_{-3}	218^{+5}_{-5}
			0.25	14.7^{+1}_{-1}	211^{+1}_{-0}
Iwasaki	1.9	0.1680	0.0	11.4^{+1}_{-1}	145^{+2}_{-2}
			0.25	11.2^{+0}_{-1}	141^{+0}_{-1}

G. Renormalized operators

To obtain the continuum values for the magnetic and electric gluon condensates, $\langle E^2 \rangle$ and $\langle B^2 \rangle$, our results obtained at finite gradient flow time need to be renormalized [49]. In general terms, the process consists of describing the flow dependence of an operator, $\mathcal{O}(x)$, via an operator product expansion for small flow times, t_g

$$\mathcal{O}(x, t_g) = \sum_i^n C_i(t_g)\mathcal{O}_i(x) + \mathcal{O}_h(t_g), \tag{34}$$

where the $C_i(t_g)$ are perturbatively calculable t_g-dependent matching (Wilson) coefficients connecting flowed operators $\mathcal{O}(x, t_g)$ to the desired renormalized local operators $\mathcal{O}_i(x)$ in a continuum scheme. The term $\mathcal{O}_h(t_g)$ captures higher-order terms of the OPE not included in the sum over i.

There is a window in flow time that must be met in order to carry out this renormalization procedure. The physical flow diffusion radius [40] $d = \sqrt{8t_g a^2}$ must satisfy two competing requirements.

First, d must remain small, such that the asymptotic expansion of perturbation theory is reliable. The flow damps momentum modes above the scale $\mu = 1/d$, where QCD is weakly coupled; the effect of these suppressed short-distance modes is absorbed into the perturbatively calculable Wilson coefficients evaluated at the scale μ.

Asymptotic freedom ensures that the strong coupling $\alpha_s(\mu)$ is small for large μ. Thus, the scale μ must be large enough that the perturbative expansion of the Wilson coefficients, $C_i(t_g)$, can be truncated at fixed loop order, a condition governed by $\alpha_s(\mu)$.

A second requirement demanding small flow times has its origin in the neglected higher-order operators in the operator product expansion, $\mathcal{O}_h(t_g)$. These contributions must be suppressed sufficiently to enable a simple t_g-dependent ansatz to capture their contribution. This second condition follows from dimensional counting, since operators of dimension $d_j > d_{\mathcal{O}_n}$ enter with coefficients suppressed by t_g raised to the power $(d_j - d_{\mathcal{O}_n})/2$, independent of the coupling.

The competing requirement in flow time is that the physical diffusion scale must be large compared to the lattice spacing so that discretization artifacts in the flowed operator, $\mathcal{O}(x, t_g)$, are suppressed. To this point in our investigation, we have determined the threshold gradient flow time where vacuum expectation values of $\mathcal{O}(x, t_g)$, namely $\langle q(x, t_g)\rangle$, $\langle E^2(x, t_g)\rangle$, and $\langle B^2(x, t)\rangle$, are under control. Herein, the somewhat coarse lattice spacing has presented some challenges. However, our use of $\mathcal{O}(a^4)$-improved operators has enabled us to obtain results at a modest flow time of $t_g \sim 1$. At this flow time, the physical dimensionful diffusion scale of the gradient flow provides $d = \sqrt{8}a$, a scale reasonably larger than the lattice spacing, providing another perspective on the required threshold flow time.

All of the aforementioned flow-time requirements encourage the consideration of small lattice spacings, particularly to meet the demands of the operator product expansion. However, with our physical lattice spacing of $a = 0.178(6)$ fm, the diffusion radius is $d = 0.50(2)$ fm, deep in the nonperturbative regime and corresponding to a scale of merely $\mu = 0.4$ GeV. Since the minimum diffusion radius required to determine $\mathcal{O}(x, t_g)$ lies beyond the scale within which perturbative matching is trustworthy, a flow-time window that simultaneously satisfies both requirements does not exist on this ensemble, and we therefore cannot proceed further.

This tension between the flow requirements is not unique to our lattices. The renormalization process has been carried out in Ref. [50] using the Wilson flow to study the SU(3) deconfinement transition. There the renormalization of the magnetic and electric gluon condensates was carried out at leading order. Using the physical critical temperature of the deconfinement transition in SU(3) Yang-Mills theory of $T_c = 290$ MeV [51], one can infer that their lattice spacings are significantly smaller than that considered here. For example, on their $N_t = 8$ lattices, the spacings are in the range 0.04 to 0.09 fm.

Even in this optimistic case, the authors concluded that extracting the renormalized gluon condensates was difficult. They found a flow-time dependence that was not accounted for in the leading-order perturbative renormalization constant. With the relevant two-loop matching coefficients now derived and under study [52–54], it would be timely to invest the significant resources required to repeat this analysis with renormalized operators in a next-generation calculation.

V. FINITE-DENSITY MODIFICATIONS OF THE GROUND-STATE FIELDS

A. Quantitative results

The conventional Wilson gauge action with two Wilson-fermion flavors is used in this research to investigate QC_2D. As presented in Sec. II, the fermion action is constructed by a gauge- and isosinglet diquark source term which lifts the low-lying eigenvalues of the Dirac operator while allowing for a controlled study of diquark condensation [30]. Recall the fermion action is

$$S_Q + S_J = \sum_{i=1,2} \bar{\psi}_i M \psi_i + \kappa j [\psi_2^{\mathrm{tr}} (C\gamma_5)\tau_2 \psi_1 - \mathrm{H.c.}], \tag{35}$$

with

$$M_{xy} = \delta_{xy} - \kappa \sum_{\nu} [(1-\gamma_\nu) e^{\mu \delta_{\nu 0}} U_\nu(x) \delta_{y,x+\hat{\nu}} + (1+\gamma_\nu) e^{-\mu \delta_{\nu 0}} U_\nu^\dagger(y) \delta_{y,x-\hat{\nu}}]. \tag{36}$$

We begin by ignoring a possible source term dependence in the results, and compare results obtained with $aj = 0(\mu = 0), aj = 0.02(a\mu = 0.25)$ and $aj = 0.04(a\mu > 0.25)$. 100–200 gauge configurations from the coarse ensemble are used at each chemical potential for this analysis. The dotted line in all the plots represents the $m_\pi/2$ phase boundary.

Figure 5 shows results for the squared chromoelectric field strength dependence on the chemical potential. Noting that increased gradient flow suppresses the chromo-electromagnetic fields, the best signals are obtained with fewer smoothing sweeps, where a clear suppression of the field strengths is manifest above $a\mu = 0.4$. The gauge field structures are suppressed at higher levels of smearing. However, all the results show the same trend; the chromo-electric field strength drops near $m_\pi/2$, but it regains strength at higher chemical potentials and becomes much stronger at the highest chemical potentials considered.

The same trend is observed for the squared chromo-magnetic field strength, as presented in Fig. 6. While this research illustrates results for very large values of the lattice chemical potential, $a\mu$, lattice artifacts are likely problematic for the largest values considered. With this in mind, we regard the most interesting region to be $a\mu \leq 0.7$. This is in agreement with earlier results, which have found that the

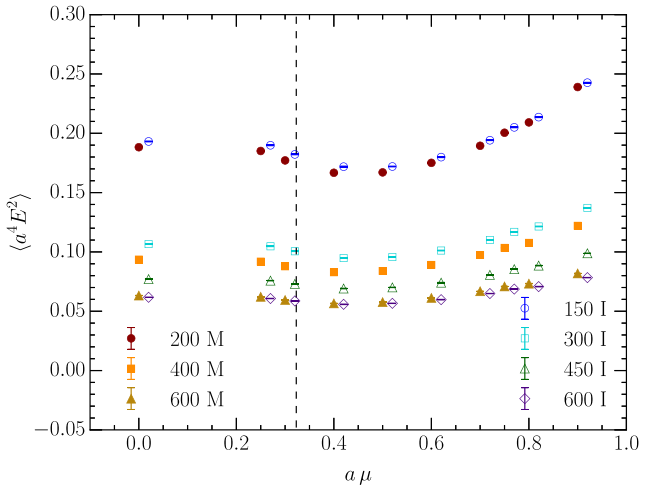


FIG. 5. Dependence of the squared chromoelectric field strength on the chemical potential. Results are illustrated for the Moran (M) and Iwasaki (I) gradient flows at several levels of smearing as indicated by the number of smearing sweeps applied with $\rho = 0.005$ in the legend. The points depicting the Iwasaki gradient flow in the plot are shifted by $a\mu = 0.02$ for clarity.

Polyakov loop increases from zero at $a\mu \gtrsim 0.7$, independent of the lattice spacing [9].

It is interesting to note how both the chromoelectric and chromomagnetic field strengths drop near $a\mu \simeq 0.3$ in advance of the anticipated phase transition at $m_\pi/2$. While it is noted that the consideration of a finite volume system necessarily creates a crossover, the concern is that the drop in advance of $m_\pi/2$ may be associated with a significant dependence on the strength of the source term. For example, if the source term acts to suppress the field strength, then an extrapolation back to zero source term would increase the field strength value, perhaps

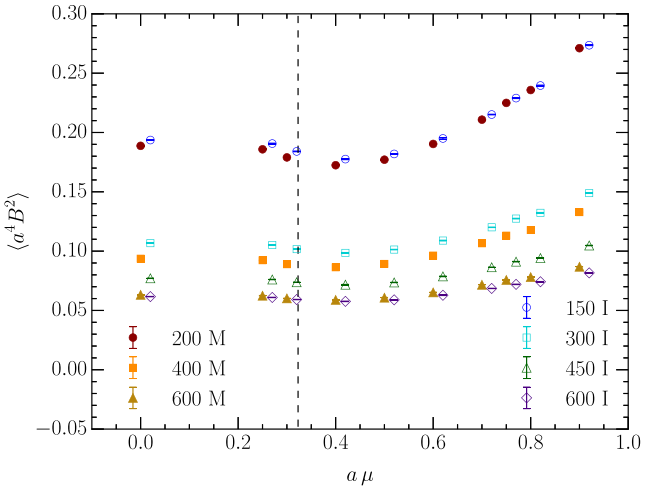


FIG. 6. The dependence of the squared chromomagnetic field strength on the chemical potential. Results are as illustrated in Fig. 5.

TABLE III. Slope parameters m_E and m_B describing the source term dependence of the squared chromoelectric and chromomagnetic field strengths as defined in Eq. (37). The results shown are obtained after 200 sweeps of Moran and 150 sweeps of Iwasaki gradient flow actions.

Gradient flow	$a\mu$	m_E	m_B
Moran (200)	0.3	0.13 ± 0.13	0.30 ± 0.13
	0.5	0.29 ± 0.13	0.35 ± 0.12
	0.7	0.09 ± 0.14	0.04 ± 0.13
	0.9	0.12 ± 0.12	0.07 ± 0.13
Iwasaki (150)	0.3	0.16 ± 0.14	0.30 ± 0.13
	0.5	0.31 ± 0.13	0.37 ± 0.12
	0.7	0.11 ± 0.14	0.04 ± 0.14
	0.9	0.09 ± 0.12	0.02 ± 0.13

maintaining the values observed at zero chemical potential. This possibility is investigated in the next Section.

B. Source term dependence

To investigate the source term dependence of the chromoelectric and chromomagnetic field strengths, we have used 50 configurations at both $aj = 0.02$ and $aj = 0.03$ for $a\mu = 0.3$, 0.5, 0.7, 0.9 in addition to the 200 configurations at $aj = 0.04$ used in the previous Section. The chromoelectric and chromomagnetic field strength dependence on the source term is modeled as

$$\langle a^4E^2\rangle = m_E\, aj + c_E, \qquad \langle a^4B^2\rangle = m_B\, aj + c_B, \tag{37}$$

where m represents the slope and c represents the y intercept.

As can be seen in Table III, the slopes are often consistent with zero, suggesting at most a weak dependence on the diquark source. Where a significant slope is found (notably at $a\mu = 0.5$), it is *positive*, $m_{E,B} \sim 0.3$.

Considering the source term value, $aj = 0.04$, used for most of the production runs, we see the correction in extrapolating back to $aj = 0$ is to *reduce* the value of the squared field strengths by ∼0.01, a very small correction on the scale of the results presented in Figs. 5 and 6. In any event, the source term dependence is not responsible for the small reduction in the field strengths ahead of the anticipated phase boundary and we conclude the effect is associated with the finite volume of the lattice.

The small magnitude of these source term corrections contrasts with the very significant corrections to the diquark condensate reported in Ref. [30], but is in accord with the very mild corrections to gluonic quantities found in Ref. [8]. Here, the corrections are an order of magnitude or more smaller than the values themselves. This source term dependence is also small relative to the smoothing dependence of the results. The magnitude is similar to the subtle differences between our calibration of the Moran and Iwasaki gradient flow algorithms. In this context, the

correction is not significant and given the large uncertainties in the source term corrections, we do not consider them further.

C. Estimating the critical chemical potential

In a finite volume system, sharp first and second order phase transitions are smoothed out to become crossovers. However, the presence and nature of a phase transition can be inferred through a systematic study of the behavior of the crossover on the spatial volume of the lattice.

A particularly useful analysis technique is to consider the sigmoid function. The function is fit to finite volume results and it has been observed that the position of the inflection point is robust against changes in the volume. In this way, the critical value for the phase transition can be estimated even in a finite volume analysis.

Therefore, fitting a sigmoid function in the datasets of the squared chromoelectric and chromomagnetic field strengths obtained will provide an estimate of the chemical potential at which a transition occurs in infinite volume.

The sigmoid function introduces four parameters which are tuned to describe the lattice results,

$$f(\mu) = c_0 + c_1 \arctan(c_2(\mu - \mu_c)). \tag{38}$$

Here, μ_c describes the position of the inflection point related to the critical value of the phase transition. Since there are four parameters in Eq. (38), at least four data points are required to find the values. In this Section, the four points selected are $a\mu = 0.00, 0.25, 0.30$ and 0.40, since these points are the closest to the estimated critical chemical potential of the phase transition; $a\mu = 0.50$ is not a feasible point to consider since it shows increases in field strengths from $a\mu = 0.40$, thus distorting the shape of the fitted sigmoid function.

The value μ_c estimates the chemical potential at which a phase transition occurs in infinite volume. As seen in Table IV, the uncertainties in the sigmoid fit for the critical $a\mu$ value increases with the number of sweeps. This happens because the higher number of sweeps increasingly distorts and suppresses the field structures, making the field strengths very similar across the transition regime. This obscures the crossovers and thus increases the uncertainties in values of the inflection points.

TABLE IV. Parameters μ_E and μ_B describe the point of inflection μ_c in the squared chromoelectric and chromomagnetic field strengths as defined in Eq. (38).

Gradient Flow	Sweeps	$a\mu_E$	$a\mu_B$
Moran	200	0.301 ± 0.002	0.295 ± 0.003
	400	0.300 ± 0.002	0.290 ± 0.004
	600	0.297 ± 0.003	0.286 ± 0.006
Iwasaki	150	0.302 ± 0.002	0.295 ± 0.003
	300	0.302 ± 0.003	0.293 ± 0.004
	450	0.302 ± 0.004	0.292 ± 0.005
	600	0.302 ± 0.005	0.293 ± 0.006

For each level of gradient flow, the values of μ_E and μ_B differ just outside the 1σ level for all the sweep numbers considered. This slight deviation may be a finite temperature effect associated with the different spatial and temporal extents of the lattice and it will be important to examine this further by considering lattices with a larger temporal extent.

In light of the chemical potentials available to us at this stage of our analysis, we are content that the sigmoid function fits support a transition at a chemical potential near the anticipated value of $am_\pi/2 = 0.323(4)$ [30].

In order to better constrain our estimate of the critical chemical potential of the phase transition, we have generated several new ensembles in the region of the finite-volume crossover. Each $16^3 \times 24$ ensemble is composed of approximately 200 gauge field configurations, with $\beta = 1.9$, $\kappa = 0.1680$, and $aj = 0.04$. We introduce the new values $a\mu = 0.28$, 0.29, 0.31, 0.32, 0.33, 0.34 and 0.35. Including our earlier ensembles at $a\mu = 0.30$ and 0.40, this gives us nine points in the transition region.

Figure 7 presents our final determination of the critical chemical potential obtained from changes in the ground-state field structure. The critical values of the chemical potentials obtained from fits to the $\langle E^2 \rangle$ and $\langle B^2 \rangle$ transitions are

$$a\mu_E = 0.325(4) \quad \text{and} \quad a\mu_B = 0.321(4), \tag{39}$$

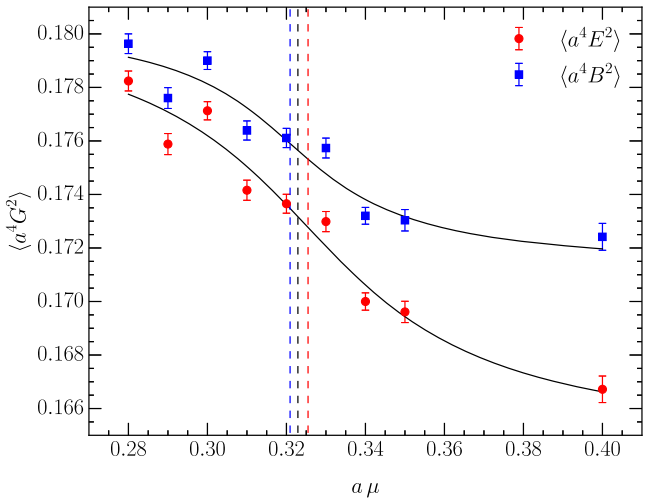


FIG. 7. Sigmoid fits to the squared chromoelectric, $\langle E^2 \rangle$, and chromomagnetic, $\langle B^2 \rangle$, field strengths obtained after Moran gradient flow at $t_g = 1.0$. This time all simulation results of the fit are in the crossover region. The vertical dashed lines report the central values of the critical chemical potentials obtained from the vacuum field structure and the expected phase boundary at $m_\pi/2$ (black dashed line).

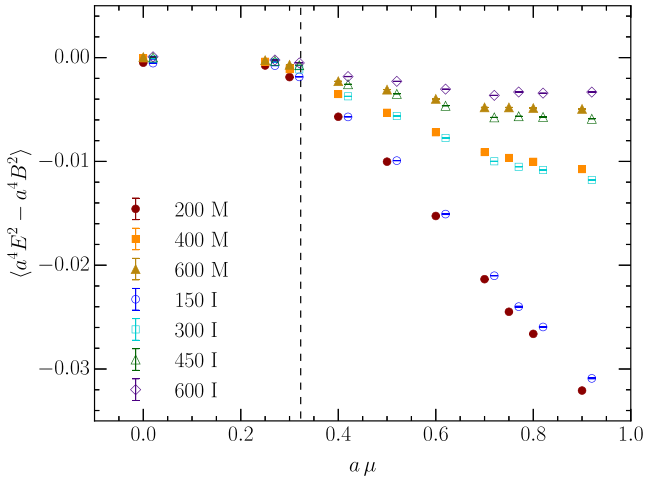


FIG. 8. Squared chromo-electromagnetic field strength difference, $\langle E^2 - B^2\rangle$, is illustrated as a function of the chemical potential, μ, for several different gradient flows. Here, both Moran (M) and Iwasaki (I) gradient flows are reported with the number of gradient-flow sweeps at $\rho = 0.005$ indicated by the preceding integer in the legend.

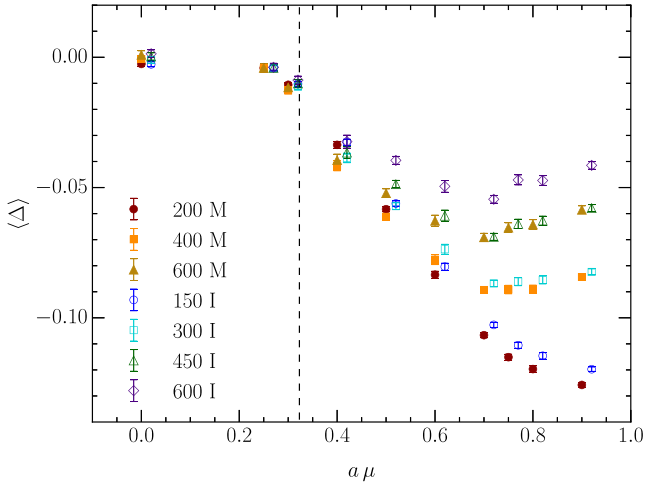


FIG. 9. Normalized chromo-electromagnetic field strength difference, $\langle\Delta\rangle$, of Eq. (40) is illustrated as a function of the chemical potential, μ, for several different gradient flows. As in Fig. 8, both Moran (M) and Iwasaki (I) gradient flows are reported with the number of gradient-flow sweeps at $\rho = 0.005$ indicated by the preceding integer in the legend.

respectively. These values are both fully consistent with the anticipated phase boundary at $am_\pi/2 = 0.323(4)$.

D. Difference in field strengths

The difference in the squared chromoelectric and the chromomagnetic field strengths further illustrates the impact of the finite chemical potential. The dependence of this difference on the gradient flow is illustrated in Fig. 8. Considering the earliest gradient flow times first, the difference in squared chromoelectric and chromomagnetic field strengths for both Moran and Iwasaki gradient flows increases monotonically as the chemical potential increases; the difference increases at a lower rate for the moderate gradient flow, before becoming approximately constant for higher numbers of sweeps. Again, lattice artifacts at the higher chemical potentials may be affecting the results. Once again we see how large gradient flow times associated with higher numbers of sweeps destroy the ground-state gauge field structures we aim to study.

To gain better intuition in quantifying the size of the effect, we introduce the normalized difference

$$\langle\Delta\rangle = \frac{\langle E^2 - B^2\rangle}{\frac{1}{2}(\langle E^2 + B^2\rangle)}. \tag{40}$$

Figure 9 shows the normalized difference plotted against the chemical potential. The difference keeps increasing in magnitude as the chemical potential increases for the lowest number of smoothing sweeps applied. However, the rate of magnitude increase in the difference drops at higher chemical potentials, perhaps due to lattice artifacts influencing measurements at the highest chemical potentials considered as we discussed previously.

Turning our attention to the results obtained following longer gradient flow trajectories, we see how excess smoothing suppresses the difference even after it has been normalized. We conclude that the process of smoothing is destroying the interesting signature of the effect of a finite chemical potential on the ground-state field structure. It is also interesting to note the different trend of the results at large chemical potentials under excess smearing.

In this regard, we recognize the importance of determining the minimum number of sweeps required to reliably and quantitatively measure the chromo-electromagnetic field strengths. Unfortunately, the quantities of interest evolve in a nontrivial manner with respect to flow time and a simple extrapolation to zero flow time is insufficient.

In this light, we conclude that our best understanding of the modification of QC_2D ground-state fields in the presence of a finite chemical potential is obtained from the lowest number of smearing sweeps consistent with stabilizing the topological charge. Moreover, we see that the Moran 200 sweep results provide the maximum signature of ground-state field structure modification. Given that further smoothing suppresses the signature, we regard the Moran 200 sweep results as optimal for gaining insight into the modification of the ground-state field structure of these ensembles.

VI. CONCLUSIONS

We have presented the first examination of both qualitative and quantitative changes in the ground-state field structure of QC_2D at finite chemical potential.

Commencing with visualizations of the subtle field structure changes, we were led to examine the differences in the chromoelectric and chromomagnetic field strengths.

Drawing on the manner in which the chemical potential is introduced into the fermion action, it was postulated that differences between the chromoelectric field strength and the chromomagnetic field strength would manifest at large values of the chemical potential. Moreover, there was some evidence that the strength of this difference would depend significantly on the methods used to measure the field strengths on the lattice.

To address this problem, we performed a careful study of the amount of smearing required for the lattice operators to provide an accurate indication of the field structure created through the Monte Carlo procedure. Two $\mathcal{O}(a^4)$-improved measures of the topological charge density with different higher-order corrections were introduced and their differences monitored as a function of smearing. Four different gradient flow actions were considered to allow an estimation of the systematic errors associated with the smoothing procedure. Dimensionless operators were created and examined to understand the underlying features of these different smoothing actions and establish smoothing thresholds for the earliest possible measurement of the chromoelectric and chromomagnetic fields. Calibrations based on the action density confirmed the veracity of these thresholds.

Examination of the chemical potential dependence of the squared field strengths confirms that minimal smoothing provides a more robust signal. This emphasizes the importance of the quantitative measures taken to determine the earliest possible gradient flow time at which one can reliably calculate the ground-state field strengths.

The results show a significant gradient flow dependence. Qualitative differences in the chemical potential dependence of the field strength measures were revealed. This prevents any attempts to extrapolate back to zero gradient flow time.

The Moran gradient flow action at 200 sweeps proved to provide the optimal signature of ground-state field structure modification. It is the earliest gradient flow time that ensures controlled systematic errors in measures of the vacuum fields. The over-improved Moran action was designed to minimize structural changes during the gradient flow. It is therefore selected as the best method for analyzing the density dependence of the ground-state SU(2) gauge field structures. Hence, in summarizing our results, we present these results in Figs. 10 through 12 as our best understanding of the modifications in ground-state field structures due to a finite matter density.

The chemical potential dependence of the ground-state field strengths is complicated. Figure 10 shows a finite-volume crossover happening near $a\mu = 0.3$ (the anticipated phase boundary), where both the chromoelectric and the chromomagnetic field strengths are suppressed. Both the field strengths reach their respective minima at $a\mu = 0.4$;

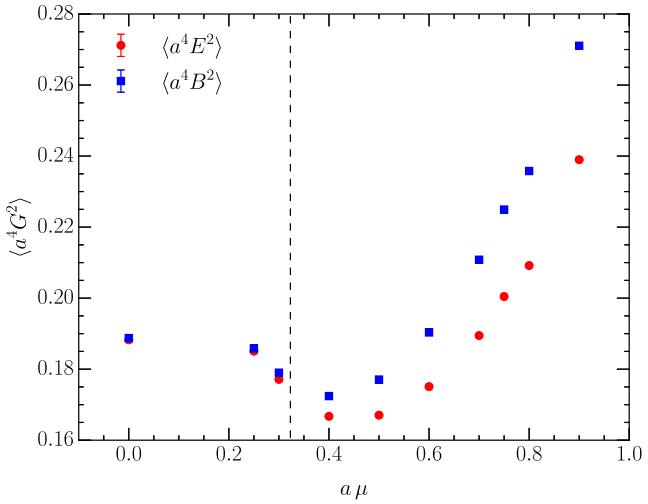


FIG. 10. Chemical potential dependence of the squared chromo-electromagnetic field strengths $\langle a^4 E^2 \rangle$ and $\langle a^4 B^2 \rangle$ at 200 sweeps of Moran gradient flow where the flow time $t_g = 1.0$.

however, at higher chemical potentials, the ground-state field strengths restore and exceed their zero chemical potential vacuum values.

The absolute squared field-strength difference, $\langle E^2 - B^2 \rangle$, is shown in Fig. 11. The point at $a\mu = 0.0$ is 2.7σ away from being zero; this is likely a small finite temperature effect associated with the different finite temporal and spatial lattice extents considered. Once again, the finite-volume crossover is observed near $a\mu = 0.3$, and the difference monotonically increases as the chemical potential increases, with the chromomagnetic field strength being consistently larger than the chromoelectric field strength.

To gain intuition and quantify the magnitude of the effect, the normalized difference, $\langle \Delta \rangle$, of Eq. (40) is

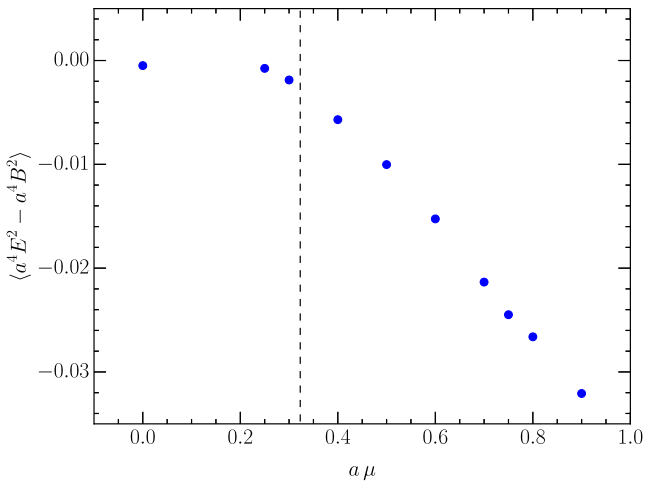


FIG. 11. Absolute difference of squared chromo-electromagnetic field strengths $\langle a^4 E^2 - a^4 B^2 \rangle$ at 200 sweeps of Moran gradient flow where the flow time $t_g = 1.0$.

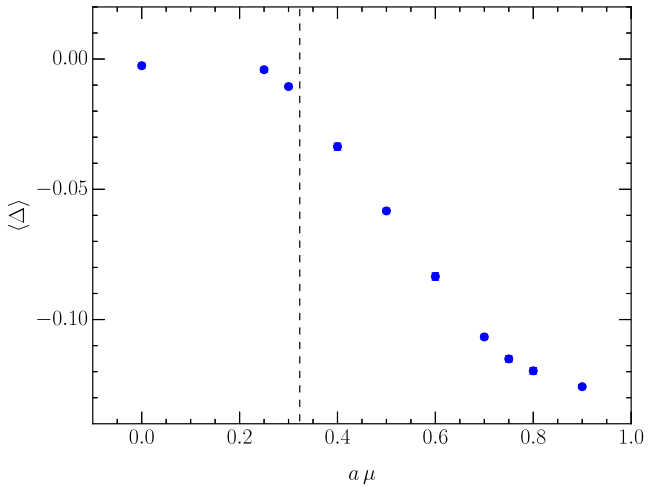


FIG. 12. The normalized difference of chromo-electromagnetic fields, $\langle\Delta\rangle$, of Eq. (40) at 200 sweeps of Moran gradient flow where the flow time $t_g = 1.0$.

constructed. This is illustrated in Fig. 12. The difference at $a\mu = 0.7$ is about 11%, which is a relatively small effect given the significant differences in the physics encountered across the phase transition. The subtlety of this effect is in accord with the early exploratory study of the distribution of topological charge density at nonzero chemical potential [25] and the more recent studies of the topological susceptibility [11,27]. The rate of increase in the normalized difference drops after $a\mu = 0.7$; however, this may be due to lattice artifacts.

We have also explored the position of the critical chemical potential of the phase transition. Here, several new ensembles were generated in the region of the finite-volume crossover. Figure 7 presents our final determinations. The critical values of the chemical potentials obtained from fits to the $\langle E^2\rangle$ and $\langle B^2\rangle$ transitions are $a\mu_E = 0.325(4)$ and $a\mu_B = 0.321(4)$, respectively, and agree with the anticipated phase boundary at $am_\pi/2 = 0.323(4)$.

In summary, the chemical potential dependence of the QC_2D ground-state field strengths is subtle. On the other hand, the nature of the observables considered provide precise results on the scale of these changes, such that clear conclusions may be drawn.

Our calculations have focused on observables that make the effect of the finite chemical potential manifest. Future quantitative calculations could explore quantities that have a more subtle dependence on the chemical potential such as the distribution of topological charge density.

Avenues for further study include the development of even more sophisticated smoothing algorithms that would allow one to study the field structure with even less smearing. The current calculations are at the threshold of being able to reveal a source-term dependence in the measures considered. Future work could provide high-statistics results that would enable one to address this systematic error. Finally, it will be fascinating to examine the extent to which the phenomena observed here extend to the three-color theory of QCD describing the strong force of nature.

ACKNOWLEDGMENTS

It is a pleasure to thank Ryan Bignell for his assistance in reading the modern file formats for the finite-density gauge-field configurations investigated herein. This work used the DiRAC Extreme Scaling service (Tursa) at the University of Edinburgh, managed by the EPCC on behalf of the STFC DiRAC HPC Facility [55]. The DiRAC service at Edinburgh was funded by BEIS, UKRI and STFC capital funding and STFC operations grants. DiRAC is part of the UKRI Digital Research Infrastructure. D. L. acknowledges support from a John and Pat Hume doctoral scholarship. This research was supported by the Australian Research Council through ARC Discovery Project Grant No. DP210103706 (D. B. L.).

DATA AVAILABILITY

The code used to generate the configurations studied herein is available via Ref. [56]. The data presented and the associated plot scripts are publicly available in Ref. [57].

[1] G. Aarts, Introductory lectures on lattice QCD at nonzero baryon number, J. Phys. Conf. Ser. **706**, 022004 (2016).
[2] J. N. Guenther, An overview of the QCD phase diagram at finite T and μ, Proc. Sci. LATTICE2021 (**2022**) 013. [arXiv:2201.02072].
[3] E. Itou, Lattice results for the equation of state in dense QCD-like theories, Universe **11**, 380 (2025).
[4] J. B. Kogut, M. A. Stephanov, D. Toublan, J. J. M. Verbaarschot, and A. Zhitnitsky, QCD—like theories at finite baryon density, Nucl. Phys. **B582**, 477 (2000).
[5] M. Creutz, Monte Carlo study of quantized SU(2) gauge theory, Phys. Rev. D **21**, 2308 (1980).
[6] S. Hands, J. B. Kogut, M.-P. Lombardo, and S. E. Morrison, Symmetries and spectrum of SU(2) lattice gauge theory at finite chemical potential, Nucl. Phys. **B558**, 327 (1999).

[7] V. V. Braguta, Phase diagram of dense two-color QCD at low temperatures, Symmetry **15**, 1466 (2023).

[8] T. Boz, S. Cotter, L. Fister, D. Mehta, and J.-I. Skullerud, Phase transitions and gluodynamics in 2-colour matter at high density, Eur. Phys. J. A **49**, 87 (2013).

[9] T. Boz, P. Giudice, S. Hands, and J.-I. Skullerud, Dense two-color QCD towards continuum and chiral limits, Phys. Rev. D **101**, 074506 (2020).

[10] N. Astrakhantsev, V. V. Braguta, E. M. Ilgenfritz, A. Y. Kotov, and A. A. Nikolaev, Lattice study of thermodynamic properties of dense QC_2D, Phys. Rev. D **102**, 074507 (2020).

[11] K. Iida, E. Itou, K. Murakami, and D. Suenaga, Lattice study on finite density QC_2D towards zero temperature, J. High Energy Phys. 10 (2024) 022.

[12] A. Begun, V. G. Bornyakov, V. A. Goy, A. Nakamura, and R. N. Rogalyov, Study of two color QCD on large lattices, Phys. Rev. D **105**, 114505 (2022).

[13] S. Hands, S. Kim, and J.-I. Skullerud, Deconfinement in dense 2-color QCD, Eur. Phys. J. C **48**, 193 (2006).

[14] K. Iida and E. Itou, Velocity of sound beyond the high-density relativistic limit from lattice simulation of dense two-color QCD, Prog. Theor. Exp. Phys. **2022**, 111B01 (2022).

[15] R. Abbott, W. Detmold, M. Illa, A. Parreño, R. J. Perry, F. Romero-López, P. E. Shanahan, and M. L. Wagman (NPLQCD Collaboration), QCD constraints on isospin-dense matter and the nuclear equation of state, Phys. Rev. Lett. **134**, 011903 (2025).

[16] E. Annala, T. Gorda, A. Kurkela, J. Nättilä, and A. Vuorinen, Evidence for quark-matter cores in massive neutron stars, Nat. Phys. **16**, 907 (2020).

[17] L. Brandes, W. Weise, and N. Kaiser, Inference of the sound speed and related properties of neutron stars, Phys. Rev. D **107**, 014011 (2023).

[18] K. Fukushima and S. Minato, Speed of sound and trace anomaly in a unified treatment of the two-color diquark superfluid, the pion-condensed high-isospin matter, and the 2SC quark matter, Phys. Rev. D **111**, 094006 (2025).

[19] F. Gross *et al.*, 50 years of quantum chromodynamics, Eur. Phys. J. C **83**, 1125 (2023).

[20] A. Cucchieri, T. Mendes, O. Oliveira, and P. J. Silva, SU(2) meets SU(3) in lattice-Landau-gauge gluon and ghost propagators, Proc. Sci. LATTICE2007 (**2007**) 322. [arXiv:0710.0344].

[21] A. Sternbeck, L. von Smekal, D. B. Leinweber, and A. G. Williams, Comparing SU(2) to SU(3) gluodynamics on large lattices, Proc. Sci. LATTICE2007 (**2007**) 340. [arXiv:0710.1982].

[22] R. Alkofer and L. von Smekal, The Infrared behavior of QCD Green's functions: Confinement dynamical symmetry breaking, and hadrons as relativistic bound states, Phys. Rep. **353**, 281 (2001).

[23] T. Boz, O. Hajizadeh, A. Maas, and J.-I. Skullerud, Finite-density gauge correlation functions in QC_2D, Phys. Rev. D **99**, 074514 (2019).

[24] B. Alles, M. D'Elia, and M. P. Lombardo, Behaviour of the topological susceptibility in two colour QCD across the finite density transition, Nucl. Phys. **B752**, 124 (2006).

[25] S. Hands and P. Kenny, Topological fluctuations in dense matter with two colors, Phys. Lett. B **701**, 373 (2011).

[26] N. Y. Astrakhantsev, V. V. Braguta, A. Y. Kotov, D. D. Kuznedelev, and A. A. Nikolaev, Lattice study of QCD at finite chiral density: Topology and confinement, Eur. Phys. J. A **57**, 15 (2021).

[27] K. Iida, E. Itou, and T.-G. Lee, Two-colour QCD phases and the topology at low temperature and high density, J. High Energy Phys. 01 (2020) 181.

[28] M. P. Lombardo, Topological aspects of dense matter: Lattice studies, Universe **7**, 336 (2021).

[29] K. Ishiguro, E. Itou, and K. Iida, Flux tube profiles in two-color QCD at low temperature and high density, Proc. Sci. LATTICE2021 (**2022**) 063. [arXiv:2111.13067].

[30] S. Cotter, P. Giudice, S. Hands, and J.-I. Skullerud, Towards the phase diagram of dense two-color matter, Phys. Rev. D **87**, 034507 (2013).

[31] K. Murakami, E. Itou, and K. Iida, Chemical potential (in) dependence of hadron scatterings in the hadronic phase of QCD-like theories and its applications, J. High Energy Phys. 02 (2024) 152.

[32] S. Hands, Lattice matter, Nucl. Phys. B, Proc. Suppl. **106**, 142 (2002).

[33] P. Hasenfratz and F. Karsch, Chemical potential on the lattice, Phys. Lett. **125B**, 308 (1983).

[34] J. B. Kogut, H. Matsuoka, M. Stone, H. W. Wyld, S. H. Shenker, J. Shigemitsu, and D. K. Sinclair, Chiral symmetry restoration in baryon rich environments, Nucl. Phys. **B225**, 93 (1983).

[35] S. Hands, S. Kim, D. Lawlor, A. Lee-Mitchell, and J.-I. Skullerud, Dense QC_2D: What's up with that?!? Proc. Sci. LATTICE2024 (**2025**) 165. [arXiv:2412.15872].

[36] S. O. Bilson-Thompson, D. B. Leinweber, and A. G. Williams, Highly improved lattice field strength tensor, Ann. Phys. (Amsterdam) **304**, 1 (2003).

[37] J. A. Mickley, W. Kamleh, and D. B. Leinweber, Numerical evidence for fractional topological objects in SU(3) gauge theory, Phys. Rev. D **109**, 094507 (2024).

[38] P. de Forcrand, M. García Pérez, and I.-O. Stamatescu, Topology of the SU(2) vacuum: A Lattice study using improved cooling, Nucl. Phys. **B499**, 409 (1997).

[39] P. de Forcrand, M. García Pérez, and I.-O. Stamatescu, Improved cooling algorithm for gauge theories, Nucl. Phys. B, Proc. Suppl. **47**, 777 (1996).

[40] M. Lüscher, Properties and uses of the Wilson flow in lattice QCD, J. High Energy Phys. 08 (2010) 071; 03 (2014) 92(E).

[41] C. Morningstar and M. J. Peardon, Analytic smearing of SU(3) link variables in lattice QCD, Phys. Rev. D **69**, 054501 (2004).

[42] F. D. R. Bonnet, D. B. Leinweber, and A. G. Williams, General algorithm for improved lattice actions on parallel computing architectures, J. Comput. Phys. **170**, 1 (2001).

[43] Y. Tanizaki, A. Tomiya, and H. Watanabe, Lattice gradient flows (de-)stabilizing topological sectors, J. High Energy Phys. 04 (2025) 123.

[44] K. Symanzik, Continuum limit and improved action in lattice theories. 2. O(N) Nonlinear sigma model in perturbation theory, Nucl. Phys. **B226**, 205 (1983).

[45] Y. Iwasaki, Renormalization group analysis of lattice Theories and improved lattice action. II. Four-dimensional non-Abelian SU(N) gauge model, arXiv:1111.7054.
[46] T. Takaishi, Heavy quark potential and effective actions on blocked configurations, Phys. Rev. D **54**, 1050 (1996).
[47] M. García Pérez, A. González-Arroyo, J. R. Snippe, and P. van Baal, Instantons from over-improved cooling, Nucl. Phys. **B413**, 535 (1994).
[48] P. J. Moran and D. B. Leinweber, Over-improved stout-link smearing, Phys. Rev. D **77**, 094501 (2008).
[49] M. Luscher and P. Weisz, Perturbative analysis of the gradient flow in non-abelian gauge theories, J. High Energy Phys. 02 (2011) 051.
[50] S. Datta, S. Gupta, and A. Lytle, Using Wilson flow to study the SU(3) deconfinement transition, Phys. Rev. D **94**, 094502 (2016).
[51] S. Borsanyi, R. Kara, Z. Fodor, D. A. Godzieba, P. Parotto, and D. Sexty, Precision study of the continuum SU(3) Yang-Mills theory: How to use parallel tempering to improve on supercritical slowing down for first order phase transitions, Phys. Rev. D **105**, 074513 (2022).
[52] R. V. Harlander, Y. Kluth, and F. Lange, The two-loop energy–momentum tensor within the gradient-flow formalism, Eur. Phys. J. C **78**, 944 (2018); **79**, 858(E) (2019).
[53] T. Iritani, M. Kitazawa, H. Suzuki, and H. Takaura, Thermodynamics in quenched QCD: Energy–momentum tensor with two-loop order coefficients in the gradient-flow formalism, Prog. Theor. Exp. Phys. **2019**, 023B02 (2019).
[54] Y. Taniguchi, S. Ejiri, K. Kanaya, M. Kitazawa, H. Suzuki, and T. Umeda (WHOT-QCD Collaboration), $N_f = 2 + 1$ QCD thermodynamics with gradient flow using two-loop matching coefficients, Phys. Rev. D **102**, 014510 (2020); **102**, 059903(E) (2020).
[55] www.dirac.ac.uk.
[56] D. Lawlor and J.-I. Skullerud, Dense QC_2D. What's up with that?!? The dataset (2024), 10.5281/zenodo.14201453.
[57] R. F. Hasan, M. Cummins, W. Kamleh, D. Lawlor, D. Leinweber, I. van Schalkwyk, and J.-I. Skullerud, Dataset for "Structure of QC_2D ground state fields at nonzero matter densities" (2026), 10.5281/zenodo.19324947.